NANO LETTERS

pubs.acs.org/NanoLett Letter

Parabolic Potential Surfaces Localize Charge Carriers in Nonblinking Long-Lifetime "Giant" Colloidal Quantum Dots

Marcell Pálmai, Joseph S. Beckwith, Nyssa T. Emerson, Tian Zhao, Eun Byoel Kim, Shuhui Yin, Prakash Parajuli, Kyle Tomczak, Kai Wang, Bibash Sapkota, Ming Tien, Nan Jiang, Robert F. Klie, Haw Yang,* and Preston T. Snee*

Cite This: *Nano Lett.* 2022, 22, 9470−9476 Read Online

ACCESS | Metrics & More | Article Recommendations | * Supporting Information

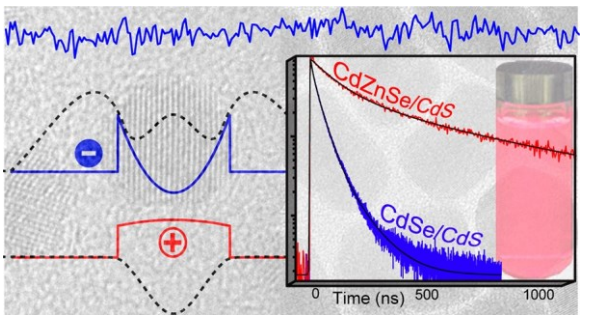

ABSTRACT: Materials for studying biological interactions and for alternative energy applications are continuously under development. Semiconductor quantum dots are a major part of this landscape due to their tunable optoelectronic properties. Size-dependent quantum confinement effects have been utilized to create materials with tunable bandgaps and Auger recombination rates. Other mechanisms of electronic structural control are under investigation as not all of a material's characteristics are affected by quantum confinement. Demonstrated here is a new structure−property concept that imparts the ability to spatially localize electrons or holes within a core/shell heterostructure by tuning the charge carrier's kinetic energy on a parabolic potential energy surface. This charge carrier separation results in extended radiative lifetimes and in continuous emission at the single-nanoparticle level. These properties enable new applications for optics, facilitate novel approaches such as time-gated single-particle imaging, and create inroads for the development of other new advanced materials.

Significant effort has been expended toward the develop- while a quasi-type II system has a single charge carrier that ment of semiconductor nanomaterials due to the potential straddles the core/shell boundary (Figure 1c).[13] None of the to impact next-generation optoelectronic applications (e.g., above PES motifs, however, allow a straightforward quantum low-cost LEDs) and biological research via imaging.[1−4] mechanical control of the radiative decay lifetime separately Nanotechnology has played a leading role, as many of the from other properties such as the bandgap. Here, we shortcomings of organic dyes and fluorescent proteins, such as demonstrate a new PES motif that significantly extends the photochemical instability, are resolved by colloidal semi- radiative lifetimes of quantum dot heterostructures through conductor quantum dots.[5] These inorganic optical reporters compositional gradients that create parabolic potential energy

are strongly absorptive and are efficient emitters with optical spectra that can be tuned from the visible to near-IR through the manipulation of size, shape, and composition of the nanomaterials.[6] Despite these demonstrations, the current technology has not realized property tunability over the full range of the optoelectronic degrees of freedom. For example, there is significant interest in extending the excited-state lifetime of optical reporters to advance new technologies in time-gated imaging and to lower the threshold for observing nonlinear phenomena such as lasing.[7−9]

surfaces for exciton charge carriers (Figure 1d). The concept was realized by synthesizing type II CdZnSe/CdS "giant" quantum dots (gQDs) where the core is composed of a graded alloy of cadmium and zinc selenide that raises the electron's kinetic energy. The electron avoids this energy penalty by fully localizing into the shell, even if the shell is composed of a higher bandgap material. This dynamic is a function of the core size and shell thickness, which imparts the ability to "dial-in" a radiative lifetime by tuning the electron−hole overlap all the

In general, core/shell heterostructured nanomaterials are classified according to the potential energy surface (PES).[10] Common examples include the type I system, in which the electron and hole are colocalized in the core by an electronically confining shell (Figure 1a). A type II structure is created through a staggered potential surface resulting in differential localizations of the charge carriers (Figure 1b),[11,12]

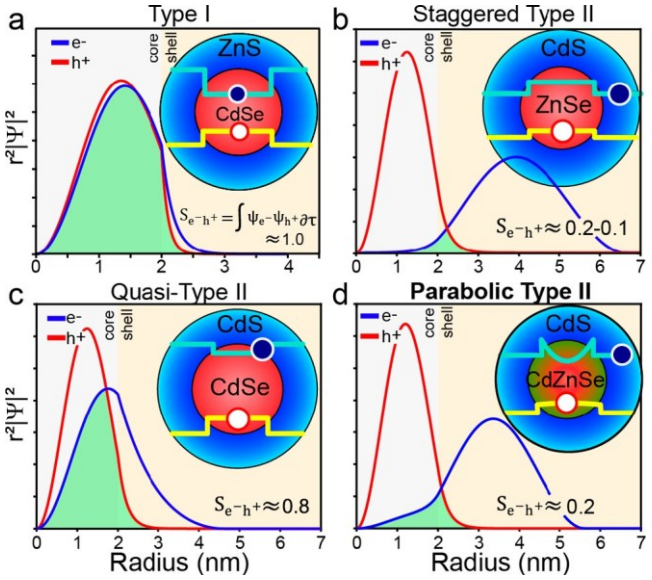

Figure 1. Electronic structure as a function of composition and morphologies of a 2 nm core with thick shell "giant" quantum dots. Solving the electron and hole radial distribution functions (RDFs) on the corresponding PES (inset) reveal structure property relationships where $S_{e\ h+}$ is the electron−hole overlap integral. (a) Type I CdSe/ZnS. (b) Type II ZnSe/CdS. (c) Quasi-type II CdSe/CdS. (d) Type II CdZnSe/CdS gQDs.

while preserving the ability of such gQDs to emit continuously and minimizing the bandgap dependence on size (Figure S28).

At the heart of the induced type II electronic structure is the compositional gradient from cadmium to zinc in the core. This was accomplished using reagents of differential reactivities; specifically, the core was prepared by coinjecting zinc oleate with highly reactive cadmium 2-hexyldecanoate into a coordinating solvent.[14] This resulted in a core with a CdSerich center that transforms into ZnSe at the exterior as revealed by energy dispersive X-ray spectroscopy (EDS) line scan analysis shown in Figure S2b. The grade in the metal composition is also evident from the fact that the 2.11 eV bandgap of a typical 6.6 ± 0.9 nm diameter core sample is larger than that expected from pure CdSe QDs,[15] which can be explained in part by an increase in the kinetic energy of the electron. It is this confinement effect that drives the electron out of the CdZnSe core upon overcoating it with a thick CdS shell. Cadmium sulfide was chosen as the shell material due to the ability to prepare very large CdZnSe/CdS gQDs as shown in Figure 2b using derivates of established wet chemical methodologies.[16−19] Notably, it was found that the SILAR method was unnecessary for the creation of thick shells and that shell growth required high temperatures toward the end of the process to realize efficient quantum yields. TEM micrographs demonstrate that CdZnSe/CdS gQDs have a uniform elongated morphology with an average length and diameter of 19.0 ± 1.6 and 13.3 ± 1.6 nm, respectively (N = 100). Additional TEM images of this sample are presented in Figure S1. The optical data of Figure 2c reveal that coating the cores results in overwhelming CdS absorptions at energies greater than the CdS bandgap (<500 nm) and a loss of core excitonic features at lower energy that are observed in Figure 1a. An EDS line scan of a single gQD reveals that the metal grading in the core structure remains intact after shelling,

https://doi.org/10.1021/acs.nanolett.2c03563
Nano Lett. 2022, 22, 9470−9476

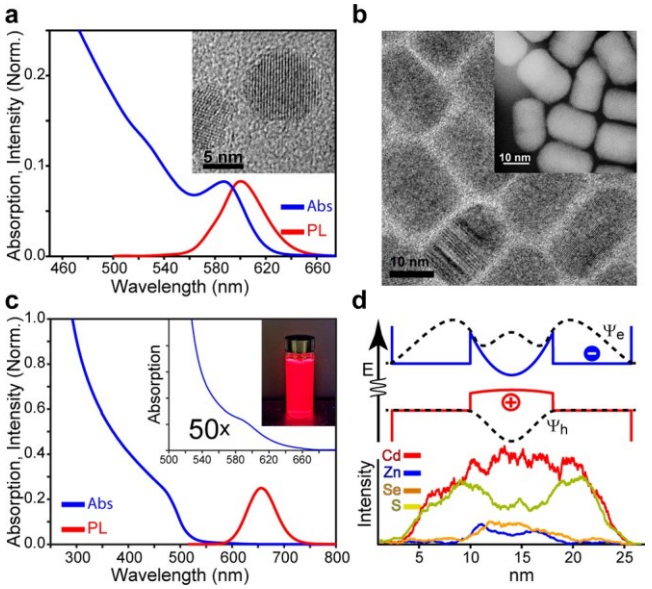

Figure 2. Physicochemical characterization and electronic structure of CdZnSe and CdZnSe/CdS gQDs. (a) Absorption and emission data of CdZnSe core QDs; data are scaled for clarity. Inset: transmission electron microscope (TEM) micrograph of core nanoparticles. (b) TEM and high-angle annular dark-field scanning transmission electron microscopy (STEM) of type II CdZnSe/CdS gQDs reveal size homogeneity and substantial shell thickness. (c) Absorption and emission data of type II CdZnSe/CdS gQDs. Absorption near the band edge is shown in the inset, additionally a typical sample under excitation. Data are scaled for clarity. (d) EDS line scan reveals retention of the core's gradient elemental composition (bottom) which creates a parabolic potential energy surface with a discontinuity at the core−shell interface (top).

which creates the potential energy landscape shown in Figure 2d.

To gain physical insights from electronic structural characterization, the Schrödinger equation was solved on the parabolic PES shown in Figure 2d using the effective mass model.[20,21] The results reveal that the charge carrier localization of a 6.9 nm diameter core CdZnSe/CdS is strongly dependent on the CdS shell thickness. As seen in the radial distribution functions in Figure 3a, both charge carriers are bound to the core when passivated meagerly. However, as the shell approaches 7 monolayers, the discontinuity at the core− shell interface results in a sharp bend in the electron's wave function as it further penetrates into the shell. This imparts higher kinetic energy, the stress from which is relieved upon electron localization into the shell as the CdS component's volume increases further. As a result, the charge carrier overlap integral plummets to ∼0.2 which is indicative of a type II nanomaterial;[20] note that the overlap of a quasi-type II CdSe/ CdS gQD is on the order of ∼0.8 (Figure S24).[18,22] Further investigations show that both the core size and shell thickness are important parameters that determine the overall electronic structure. The charge carriers of type II CdZnSe/CdS gQDs with large cores experience minimal confinement energies, and as such, there is less probability density for the electron to localize within the shell as shown in Figure 3b. The resulting charge carriers' colocalization in the core is evident from high (>0.9) overlap integrals shown in Figure 3c. Shrinking the CdZnSe cores increases the electron kinetic energy such that shell localization becomes favorable as discussed above.

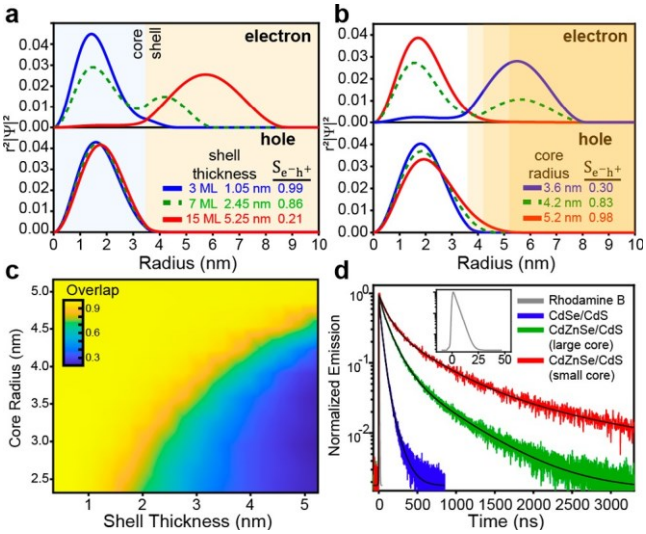

Figure 3. Effective mass calculations on the electronic structure and time-resolved emission of CdZnSe/CdS QDs. (a) RDFs of the electron and hole as a function of shell thickness reveal electron localization in CdS past a shell thickness threshold. (b) Charge carrier RDFs of CdZnSe/CdS QDs as a function of core radius reveal the onset of type II character as the core becomes smaller, while the hole experiences minimal penetration into the shell. All calculations used a variable shell thickness to simulate a 16 nm diameter particle. (c) Heatmap of electron/hole overlap of CdZnSe core radius vs CdS shell thickness reveals type II behavior (blue) is more accessible with smaller CdZnSe cores. (d) Time-resolved photoluminescence decay of type II CdZnSe/CdS gQDs compared to control CdSe/CdS gQDs and the fluorescent dye Rhodamine B (inset). Average lifetimes of type II CdZnSe/CdS gQDs are substantially longer than organic dyes or control CdSe/CdS gQDs and are correlated to the core bandgap as predicted theoretically.

Additionally, models that include the effects of alloying the CdZnSe core and CdS shell retain the type I to type II transition; further details are provided in the Supporting Information. As these calculations were performed with spherical models, the electronic effects due to nanoparticle asymmetry shown in Figure 2b were studied. As discussed in the Supporting Information, effective mass modeling of high aspect ratio 13 nm × 19 nm core/shell models retain a

https://doi.org/10.1021/acs.nanolett.2c03563
Nano Lett. 2022, 22, 9470−9476

type II electronic structure as revealed by differential charge carrier localization with a resulting overlap of 0.23.

These calculations predict a much-prolonged radiative lifetime because the radiative rate is proportional to the overlap integral via $(\tau_{rad})^{-1} \propto (S_{eh^+})^2$.[23] This is supported by time-resolved emission studies within the linear excitation power region as shown in Figure 3d (see Figures S7−S20 for power dependence studies). The average lifetimes among the various type II CdZnSe/CdS gQDs prepared in this study vary from 150 → 520 ns, which is longer than observed in CdSe/CdS and is more similar to type II ZnSe/CdS gQD control samples; see the Supporting Information for a full comparison. CdZnSe/CdS samples prepared using higher bandgap cores were found to have longer lifetimes, which is consistent with the trends predicted in Figure 3c. Data on representative samples are provided in Table S1. Last, electronic structure calculations reveal the potential to apply this paradigm to several other material systems that can sequester either holes or electrons into thick shells (Figure S29).

Beyond empowering much sought-after lifetime tunability, the parabolic PES concept also provides a mechanism to relate electronic structure to photophysical properties such as emission intermittency (i.e., blinking). This single-particle phenomenon is a serious drawback for imaging and tracking applications,[24] which is why quasi-type II CdSe/CdS gQDs generated significant interest due (in part) to the fact that these optical reporters may emit continuously. Subsequent investigations into this intriguing behavior led to several proposed mechanisms that may be grouped under the paradigms of surface trap state suppression and reduced Auger recombination of charged QDs.[25] While the former can be achieved through careful synthesis during shell formation, the latter is determined by the material's electronic structure. In CdSe/CdS gQDs, two mechanistic models have been proposed to explain the Auger dynamics. One predicates that the efficiency of the Auger process is affected by overlap between the exciton ground state and the electron's ionized free-wave state. Thus, Auger ionization is subdued in materials with a smooth PES between the core and shell due to minimization of this overlap (Figure 4a).[26−31] Along this line, many reports have demonstrated suppression of Auger ionization by virtue of alloying of the core and shell at their interface.[29−31] The other model, Figure 4b, reasons that Auger

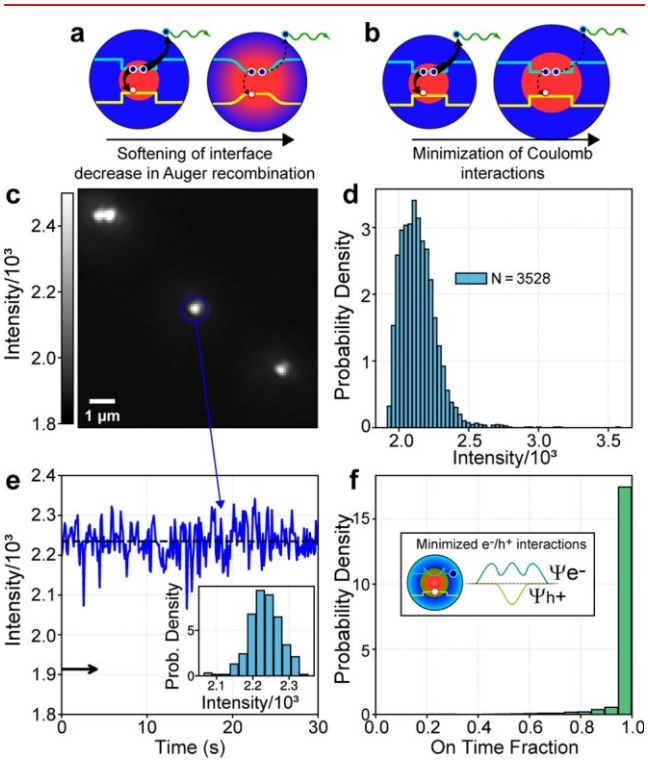

Figure 4. Testing emission intermittency models. Cartoons illustrating the smooth-potential (a) and the interaction minimization (b) models for suppressing Auger dynamics. (c) Representative single gQD image. (d) Particle-by-particle intensity distribution showing a near-uniform emission intensity per particle. (e) Typical singleparticle emission trajectory of type II CdZnSe/CdS gQDs shows no blinking behavior (117 ms bin). The horizontal arrow indicates the background level. Inset: Intensity distribution of this time trajectory. (f) Histogram of the on-time distribution of the same sample (3528 particles). For a comparison of the blinking behavior with quasi-type II gQDs, see Figure S23.

suppression may result from minimization of exciton charge carrier interactions within the large volume of gQDs.[32−34]

The generality of the two competing models can be examined using the parabolic PES gQDs. At the single-particle level, the smooth-potential model predicts significant emission intermittency because of the discontinuity at the core/shell interface of the parabolic PES. However, as shown in Figure 4c−f, type II CdZnSe/CdS gQDs are nonblinking. These results thus support the charge carrier separation model for Auger dynamics suppression. This is consistent with the fact that type II heterostructures are known to have long biexciton lifetimes due to slower Auger recombination rates.[34] We posit that screening the interaction of the charge carriers due to the increased dielectric of the ZnSe interfacial component also plays a role.[35,36]

"Giant" CdZnSe/CdS semiconductor heterostructures with parabolic potential energy surfaces as created by alloyed cores in the core/shell structure impart a fully type

https://doi.org/10.1021/acs.nanolett.2c03563
Nano Lett. 2022, 22, 9470−9476

II electronic structure. This affords radiative lifetime tunability beyond what has been previously demonstrated in "quasi-type II" systems. Such property control enables new experimental realizations in imaging,[37] for example, whereby the enhanced lifetimes enable background removal via time gating while single-particle tracking is facilitated by the nanoparticles' continuous emission. Furthermore, the demonstration of continuous emission from such particles adds to the storehouse of knowledge concerning the electronic properties that result in suppression of emission intermittency. Consequently, the development of a novel method to impart a type II electronic structure by shaping the potential surface creates inroads for engineering new material systems with designer properties. This realization will be facilitated by the prediction that several binary, ternary, and especially cadmium-free semiconductor heterostructures can be incorporated into the electronic structural paradigm presented here.

METHODS

Chemicals. Sulfur powder (S, 99.98%), cadmium acetate dihydrate ($Cd(CH_3COO)_2 \cdot 2H_2O$, ≥98.0%) oleic acid (OA, 90%), oleylamine (90%), 1-octadecene (ODE, 90%), and zinc oxide (ZnO, nanopowder, <100 nm particle size) were purchased from Sigma-Aldrich. 2-Hexyldecanoic acid (>98.0%) was purchased from TCI. Selenium (Se, 99.99%) and trioctylphosphine (TOP, 97%) were obtained from Strem. Cadmium oxide brown (CdO, ≥99.0%) was purchased from Fluka. Cadmium acetate was recrystallized from acetic acid and heat dried under vacuum. Oleic acid was recrystallized prior to use. Oleylamine was purified by vacuum distillation and was stored under inert atmosphere. All other reagents were used as received. Syntheses of precursors and control samples are available in the Supporting Information.

Synthesis of CdZnSe Cores. Core CdZnSe QDs were prepared by a derivative of a method described previously.[38] The Cd precursor, cadmium(2-hexyldecanoate)$_2$, was designed to be more reactive to selenium over zinc(oleate)$_2$ to create a gradient in the core QD structure. Typically, 36 mg (0.28 mmol) of CdO, 0.156 g (0.178 mL, 0.61 mmol) of 2hexyldecanoic acid, and 5 mL of ODE were added into a 50 mL three-neck round-bottom flask and heated at 100 °C under vacuum for 1 h. After, the solution was heated to 280 °C under an inert N_2 atmosphere for 15 min to yield a clear albeit slightly discolored solution, cooled back to 100 °C, and degassed again. Finally, the temperature was increased to 310 °C, 1 mL of 1.0 M TOPSe together with 0.71 g of zinc oleate/ ODE solution was quickly injected, and the QDs were grown at 280 °C for 20 min and at 300 °C for 10 min. The emission ranged between 580 → 620 nm for the samples prepared in this study. Data in the main text were derived from smaller 6.6 ± 0.9 nm core (Em: 590 nm) and larger 6.9 ± 0.6 nm core (Em: 617 nm) samples that were subsequently overcoated with CdS as described below.

Synthesis of Type II CdZnSe/CdS gQDs. The process is a variation of previously published procedures.[16−19] A fourneck 100 mL reaction flask was charged with 1.0×10^{-7} mol processed core CdZnSe QDs in hexanes, 4 mL of oleylamine, and 4 mL of ODE. The hexanes were removed at 60 °C under reduced pressure. Next, the temperature was increased to 220 °C under an inert N_2 atmosphere, and a syringe injector was used to add the precursors for shell growth. The shelling was performed via simultaneous coinjection of the cadmium and sulfur solutions over the course of 2 days, ∼7 h each day. The cadmium and sulfur precursors were of equal concentration, typically ∼7 mL of 0.1875 M, and were injected at a rate of 1 mL/h. The temperature was increased incrementally starting from 220 to 310 °C over the course of the shelling process. Afterward, the sample was cooled to room temperature and processed with size selective precipitation prior to analyses. Quantum yields ranged from 15% → 32%.

Size Selective Precipitation of gQDs. In a typical procedure, half of the gQDs were precipitated by adding 10 mL of methanol and 10 mL of isopropanol and centrifuged (15 min, 3500 rpm) to isolate the products from the supernatant. The gQDs were redispersed in 5−10 mL of hexane, followed by the addition of isopropanol dropwise until the solution became slightly turbid. Then, the mixture was centrifuged (5 min, 1500 rpm), the supernatant was discarded, and the pellet was dried under ambient conditions. Finally, gQDs were redispersed in 4.0 g of ODE and 0.5 g of OA as a stabilizing surfactant and stored under ambient conditions.

Wave Function Overlap. Effective mass calculations were performed using the paradigm of Şahin et al.,[21] whereby the effective mass varies radially to reflect the composition. As a result, solving the Schrödinger equation is not straightforward as the solutions are not spherical Bessel functions; readers are directed to ref 20 for additional details. The finite difference method was used to solve the Schrödinger equation and electrostatic potentials as determined by Poisson's equation. BenDaniel-Duke boundary conditions at interfaces were enforced.[39] The electrostatic potential as calculated by Poisson's equation using the finite difference method requires normalization. This was accomplished by scaling the potential at a distance >3 × radius to match that of Coulomb's Law using the dielectric of toluene (ε = 2.38): $= \frac{\pm e}{4\pi\varepsilon\varepsilon_0 r}$.

MATLAB was used for all calculations.

https://doi.org/10.1021/acs.nanolett.2c03563
Nano Lett. 2022, 22, 9470−9476

Time-Resolved Spectroscopy and Analysis. QDs were dispersed in hexanes prior to optical measurements at room temperature. Fluorescence spectra were recorded using a HORIBA FluoroMax-4 spectrofluorometer. UV/vis spectroscopy measurements were performed with a Varian Cary 300 Bio spectrophotometer. Quantum yields were determined in comparison to organic dye standards. TCSPC data for Figure 4 was collected using a HORIBA-Jobin Yvon FluoroMax-3 spectrometer using a 445 nm pulsed laser diode light source (HORIBA-Jobin Yvon, NanoLED-450) for excitation. For power-dependent experiments, the TCSPC data was collected for flux levels below 0.1 $\mu J/cm^2$ using the same FluoroMax-3 and at higher fluxes using an upright microscope system described previously[37] with 400 nm excitation accomplished by the doubling of 800 nm in a BBO crystal. QDs were dispersed in hexanes to an absorbance of below 0.05 at the lowest energy absorption peak, and the same solution was used for both flux ranges. Uncertainty in fit parameters was derived from 2000 bootstrapped samples.

Analysis of QD Photoluminescence Decays. The analysis of QD photoluminescence decays was accomplished by the comparison of the data to a multiexponential model defined as

$$I(t) = bkg + I_0 \sum_i a_i \times \exp\left(-\frac{t}{\tau_i}\right)$$

where bkg is a background offset, I_0 represents the initial intensity, and a_i and τ_i represent the relative amplitudes and lifetimes, respectively, of the multiexponential, and $\Sigma_i a_i = 1$. The use of $i = 3$ yielded good fits. The characteristic time of the trace $\langle\tau\rangle$ was determined as

$$\langle\tau\rangle = \sum_i |a_i| \times \tau_i$$

Emission Intermittency Experiment and Analysis. All QD samples were diluted in hexanes to ~25 pM concentration and were spun (70 s, 1500 rpm) onto a glass coverslip for observation under an epi-fluorescence microscope. An Ex: 427/10 nm, Em: 570 nm LP filter set was used with an exposure time of 100 ms. The data analysis methodology is divided into spot identification and intensity analysis. Both are described below.

Spot Identification. There are three key steps in the process for identifying individual quantum dot emitters. First, we use a bandpass filter to suppress camera readout noise and any multipixel length noise. This filtered data is then binarized using a threshold determined using Otsu's method,[40] and spots are identified as bright pixels that are connected by 8 vertices to other bright pixels. The center of the spot is defined as the center of the individually identified centroids.

Intensity Analysis. Once the spots are identified, the mean intensity of a 4 × 4 square centered on the spot is taken at each frame time t and is defined as the intensity of the QD. This is compared to the background intensity at each time t. The background intensity is computed using the following procedure. First, 4 × 4 squares of the intense spot locations are removed from the image and the mean of the remaining values is taken to be the background intensity. The μ and σ of this distribution (the distributions of the background photons pass the Kolmogorov−Smirnov test for normality) are then used to calculate a threshold for the hypothesis test that the intensity of the spot at time t is drawn from the background distribution or another distribution.[41] In detail, this is the same as deciding between two hypotheses: H_1 if the intensity is drawn from the QD emission[42] distribution and H_0 if it is drawn from the background distribution. The distribution of emission intensity as recorded by our camera is modeled as Gaussian, denoted as $N(\mu,\sigma)$ with μ and σ being the mean and standard deviation, respectively. This is accomplished by observing the value of average spot intensity T at time t and deciding H_1 if $T > \gamma'$ and H_0 otherwise. That is, a thresholdbased statistical test is applied to determine if the experimentally determined T belongs to the $N(\mu_1, \sigma)$ distribution (H_1) or to the $N(\mu_0, \sigma)$ distribution (H_1) with $\mu_1 > \mu_0$. An optimal threshold γ' for the test based on an prescribed false positive rate (α, here 0.05) is determined using[41]

$$\gamma' = Q^{-1}(\alpha) + \mu_0$$

where $Q^{-1}(\alpha)$ is the inverse $Q(\cdot)$ function. The $Q(\cdot)$ function is the tail distribution of the standard Gaussian and analytically can be represented as

$$Q(x) = 0.5 \times \mathrm{erfc}(x/\sqrt{2})$$

where erfc(·) is the complementary error function. The state is determined to be on or off depending on a comparison of the intensity state value versus the threshold γ' for each identified change point[42,43] in the intensity trace. The on-time is then computed as N_{on}/N_{off}, where N_{on} and N_{off} are the number of data points spent in the on and off states, respectively.

Structural Characterization. Scanning Transmission Electron Microscopy (STEM) images were obtained on an aberration-corrected JEOL JEMARM 200CF electron microscope operating at 200 kV using a cold field emission source. Atomic-resolution imaging is achieved with a probe convergence semiangle of 25 mrad yielding a probe size of approximately 0.078 nm. High angle annular dark field

https://doi.org/10.1021/acs.nanolett.2c03563
Nano Lett. 2022, 22, 9470−9476

(HAADF) imaging utilized an inner collecting angle of 68 mrad and outer collecting angle of 230 mrad; annular bright field (ABF) imaging was performed with an inner collecting angle of 11 mrad and outer collecting angle of 22 mrad. Other images shown in the Supporting Information were obtained using a JEOL JEM-3010 operating at 300 keV. A 300-mesh gold grid was used for nanoparticle imaging.

ASSOCIATED CONTENT

*** Supporting Information**

The Supporting Information is available free of charge at https://pubs.acs.org/doi/10.1021/acs.nanolett.2c03563.

Additional experimental notes on precursor and control sample syntheses; additional characterization data from TEM, optical analyses including time-resolved emission and Raman spectroscopy, and details of the effective mass calculations including the split operator method
(PDF)

AUTHOR INFORMATION

Corresponding Authors

Haw Yang − *Department of Chemistry, Princeton University, Princeton, New Jersey 08544-0001, United States;* orcid.org/0000-0003-0268-6352; Email: hawyang@princeton.edu

Preston T. Snee − *Department of Chemistry, University of Illinois Chicago, Chicago, Illinois 60607-7061, United States;* orcid.org/0000-0002-6544-6826; Email: sneep@ uic.edu

Authors

Marcell Pálmai − *Department of Chemistry, University of Illinois Chicago, Chicago, Illinois 60607-7061, United States*

Joseph S. Beckwith − *Department of Chemistry, Princeton University, Princeton, New Jersey 08544-0001, United States;* orcid.org/0000-0003-4726-230X

Nyssa T. Emerson − *Department of Chemistry, Princeton University, Princeton, New Jersey 08544-0001, United States;* orcid.org/0000-0002-6903-0692

Tian Zhao − *Department of Chemistry, Princeton University, Princeton, New Jersey 08544-0001, United States*

Eun Byoel Kim − *Department of Chemistry, University of Illinois Chicago, Chicago, Illinois 60607-7061, United States*

Shuhui Yin − *Department of Chemistry, Princeton University, Princeton, New Jersey 08544-0001, United States*

Prakash Parajuli − *Department of Physics, University of Illinois Chicago, Chicago, Illinois 60607-7059, United States*

Kyle Tomczak − *Department of Chemistry, University of Illinois Chicago, Chicago, Illinois 60607-7061, United States*

Kai Wang − *Department of Chemistry, University of Illinois Chicago, Chicago, Illinois 60607-7061, United States*

Bibash Sapkota − *Department of Physics, University of Illinois Chicago, Chicago, Illinois 60607-7059, United States*

Ming Tien − *Department of Biochemistry and Molecular Biology, Pennsylvania State University, University Park, Pennsylvania 16802-1503, United States;* orcid.org/0000-0003-0257-2347

Nan Jiang − *Department of Chemistry, University of Illinois Chicago, Chicago, Illinois 60607-7061, United States;* orcid.org/0000-0002-4570-180X

Robert F. Klie − *Department of Physics, University of Illinois Chicago, Chicago, Illinois 60607-7059, United States;* orcid.org/0000-0003-4773-6667

Complete contact information is available at: https://pubs.acs.org/10.1021/acs.nanolett.2c03563

Author Contributions

M.P. developed the synthesis of type II CdZnSe/CdS and control CdSe/CdS gQDs and assisted with the preparation of the manuscript. J.S.B., N.T.E., and S.Y. performed single nanoparticle spectroscopy. J.S.B. measured all TCSPC data taken on the Fluorolog instrument. T.Z. measured TCSPC data using the upright microscope. J.S.B. analyzed all TCSPC data. E.B.K. and N.T.E. collected and analyzed TEM data, while P.P., B.S., and R.F.K. collected and examined HAADFSTEM images and performed EDS elemental analyses. K.T. assisted with reagent syntheses. K.W. and N.J. assisted with Raman characterizations. M.T. and H.Y. helped design experiments and H.Y. supervised single QD spectroscopy and lifetime measurements. P.T.S. conceived the type II structure, performed theoretical modeling, and assisted with the manuscript preparation. All coauthors participated in scientific discussions of this work as well as editing the manuscript.

Notes

The authors declare no competing financial interest.

https://doi.org/10.1021/acs.nanolett.2c03563
Nano Lett. 2022, 22, 9470−9476

ACKNOWLEDGMENTS

Startup funding to P.T.S. from the University of Illinois Chicago primarily supported this work, while acknowledgment is made to the Donors of the American Chemical Society Petroleum Research Fund for partial support of this research. The U.S. Department of Energy is gratefully acknowledged for financial support (Grant No. DE-SC0019364 to H.Y., M.T., and P.T.S.). J.S.B. acknowledges the Fonds National Suisse de la Recherche Scientifique for financial support in the form of an Early Postdoc Mobility grant (Project No. P2GEP2_191208). N.J. acknowledges support from the National Science Foundation (No. CHE-1944796).

REFERENCES

(1) Shen, H.; Gao, Q.; Zhang, Y.; Lin, Y.; Lin, Q.; Li, Z.; Chen, L.; Zeng, Z.; Li, X.; Jia, Y.; Wang, S.; Du, Z.; Li, L. S.; Zhang, Z. Visible Quantum Dot Light-Emitting Diodes with Simultaneous High Brightness and Efficiency. *Nature Photon* 2019, *13* (3), 192−197.

(2) García de Arquer, F. P.; Talapin, D. V.; Klimov, V. I.; Arakawa, Y.; Bayer, M.; Sargent, E. H. Semiconductor Quantum Dots: Technological Progress and Future Challenges. *Science* 2021, *373* (6555), eaaz8541.

(3) Hildebrandt, N.; Spillmann, C. M.; Algar, W. R.; Pons, T.; Stewart, M. H.; Oh, E.; Susumu, K.; Díaz, S. A.; Delehanty, J. B.; Medintz, I. L. Energy Transfer with Semiconductor Quantum Dot Bioconjugates: A Versatile Platform for Biosensing, Energy Harvesting, and Other Developing Applications. *Chem. Rev.* 2017, *117* (2), 536−711.

(4) Wang, W.; Mattoussi, H. Engineering the Bio−Nano Interface Using a Multifunctional Coordinating Polymer Coating. *Acc. Chem. Res.* 2020, *53* (6), 1124−1138.

(5) Resch-Genger, U.; Grabolle, M.; Cavaliere-Jaricot, S.; Nitschke, R.; Nann, T. Quantum Dots versus Organic Dyes as Fluorescent Labels. *Nat. Methods* 2008, *5* (9), 763−775.

(6) Efros, A. L.; Brus, L. E. Nanocrystal Quantum Dots: From Discovery to Modern Development. *ACS Nano* 2021, *15* (4), 6192−6210.

(7) García-Santamaría, F.; Chen, Y.; Vela, J.; Schaller, R. D.; Hollingsworth, J. A.; Klimov, V. I. Suppressed Auger Recombination in "Giant" Nanocrystals Boosts Optical Gain Performance. *Nano Lett.* 2009, *9* (10), 3482−3488.

(8) Keller, A. M.; Ghosh, Y.; DeVore, M. S.; Phipps, M. E.; Stewart, M. H.; Wilson, B. S.; Lidke, D. S.; Hollingsworth, J. A.; Werner, J. H. 3-Dimensional Tracking of Non-Blinking 'Giant' Quantum Dots in Live Cells. *Adv. Funct. Mater.* 2014, *24* (30), 4796−4803.

(9) Jung, H.; Ahn, N.; Klimov, V. I. Prospects and Challenges of Colloidal Quantum Dot Laser Diodes. *Nat. Photonics* 2021, *15* (9), 643−655.

(10) Dorfs, D.; Hickey, S.; Eychmüller, A.Type-I and Type-II Core− Shell Quantum Dots: Synthesis and Characterization. In *Nanotechnologies for the Life Sciences*; American Cancer Society, 2011; DOI: 10.1002/9783527610419.ntls0199.

(11) Kim, S.; Fisher, B.; Eisler, H. J.; Bawendi, M. Type-II Quantum Dots: CdTe/CdSe(Core/Shell) and CdSe/ZnTe(Core/Shell) Heterostructures. *J. Am. Chem. Soc.* 2003, *125* (38), 11466−11467.

(12) Nemchinov, A.; Kirsanova, M.; Hewa-Kasakarage, N. N.; Zamkov, M. Synthesis and Characterization of Type II ZnSe/CdS Core/Shell Nanocrystals. *J. Phys. Chem. C* 2008, *112* (25), 9301−9307.

(13) Zhu, H.; Song, N.; Rodríguez-Córdoba, W.; Lian, T. Wave Function Engineering for Efficient Extraction of up to Nineteen Electrons from One CdSe/CdS Quasi-Type II Quantum Dot. *J. Am. Chem. Soc.* 2012, *134* (9), 4250−4257.

(14) Yang, Y.; Qin, H. Y.; Jiang, M. W.; Lin, L.; Fu, T.; Dai, X. L.; Zhang, Z. X.; Niu, Y.; Cao, H. J.; Jin, Y. Z.; Zhao, F.; Peng, X. G. Entropic Ligands for Nanocrystals: From Unexpected Solution Properties to Outstanding Processability. *Nano Lett.* 2016, *16* (4), 2133−2138.

(15) Yu, W. W.; Qu, L. H.; Guo, W. Z.; Peng, X. G. Experimental Determination of the Extinction Coefficient of CdTe, CdSe, and CdS Nanocrystals. *Chem. Mater.* 2003, *15* (14), 2854−2860.

(16) Ghosh, Y.; Mangum, B. D.; Casson, J. L.; Williams, D. J.; Htoon, H.; Hollingsworth, J. A. New Insights into the Complexities of Shell Growth and the Strong Influence of Particle Volume in Nonblinking "Giant" Core/Shell Nanocrystal Quantum Dots. *J. Am. Chem. Soc.* 2012, *134* (23), 9634−9643.

(17) Welsher, K.; McManus, S. A.; Hsia, C.-H.; Yin, S.; Yang, H. Discovery of Protein- and DNA-Imperceptible Nanoparticle Hard Coating Using Gel-Based Reaction Tuning. *J. Am. Chem. Soc.* 2015, *137* (2), 580−583.

(18) Mahler, B.; Spinicelli, P.; Buil, S.; Quelin, X.; Hermier, J.-P.; Dubertret, B. Towards Non-Blinking Colloidal Quantum Dots. *Nat. Mater.* 2008, *7* (8), 659−664.

(19) Li, J. J.; Wang, Y. A.; Guo, W.; Keay, J. C.; Mishima, T. D.; Johnson, M. B.; Peng, X. Large-Scale Synthesis of Nearly Monodisperse CdSe/CdS Core/Shell Nanocrystals Using Air-Stable Reagents via Successive Ion Layer Adsorption and Reaction. *J. Am. Chem. Soc.* 2003, *125* (41), 12567−12575.

(20) Gentle, C. M.; Wang, Y.; Haddock, T. N.; Dykstra, C. P.; van der Veen, R. M. Internal Atomic-Scale Structure Determination and Band Alignment of II–VI Quantum Dot Heterostructures. *J. Phys. Chem. C* 2020, *124* (6), 3895−3904.

(21) Şahin, M.; Nizamoglu, S.; Yerli, O.; Volkan Demir, H. Reordering Orbitals of Semiconductor Multi-Shell Quantum DotQuantum Well Heteronanocrystals. *J. Appl. Phys.* 2012, *111* (2), 023713.

(22) Chen, Y.; Vela, J.; Htoon, H.; Casson, J. L.; Werder, D. J.; Bussian, D. A.; Klimov, V. I.; Hollingsworth, J. A. Giant" Multishell CdSe Nanocrystal Quantum Dots with Suppressed Blinking. *J. Am. Chem. Soc.* 2008, *130* (15), 5026−5027.

(23) Rajadell, F.; Climente, J. I.; Planelles, J. Excitons in Core-Only, Core-Shell and Core-Crown CdSe Nanoplatelets: Interplay between in-Plane Electron-Hole Correlation, Spatial Confinement, and Dielectric Confinement. *Phys. Rev. B* 2017, *96* (3), 035307.

(24) Rose, K. A.; Molaei, M.; Boyle, M. J.; Lee, D.; Crocker, J. C.; Composto, R. J. Particle Tracking of Nanoparticles in Soft Matter. *J. Appl. Phys.* 2020, *127* (19), 191101.

(25) Yuan, G.; Gómez, D. E.; Kirkwood, N.; Boldt, K.; Mulvaney, P. Two Mechanisms Determine Quantum Dot Blinking. *ACS Nano* 2018, *12* (4), 3397−3405.

(26) Cragg, G. E.; Efros, A. L. Suppression of Auger Processes in Confined Structures. *Nano Lett.* 2010, *10* (1), 313−317.

(27) Park, Y.-S.; Lim, J.; Makarov, N. S.; Klimov, V. I. Effect of Interfacial Alloying versus "Volume Scaling" on Auger Recombination in Compositionally Graded Semiconductor Quantum Dots. *Nano Lett.* 2017, *17* (9), 5607−5613.
(28) Efros, A. L.; Nesbitt, D. J. Origin and Control of Blinking in Quantum Dots. *Nature Nanotechnol* 2016, *11* (8), 661−671.
(29) Nasilowski, M.; Spinicelli, P.; Patriarche, G.; Dubertret, B. Gradient CdSe/CdS Quantum Dots with Room Temperature Biexciton Unity Quantum Yield. *Nano Lett.* 2015, *15* (6), 3953−3958.
(30) Bae, W. K.; Padilha, L. A.; Park, Y.-S.; McDaniel, H.; Robel, I.; Pietryga, J. M.; Klimov, V. I. Controlled Alloying of the Core−Shell Interface in CdSe/CdS Quantum Dots for Suppression of Auger Recombination. *ACS Nano* 2013, *7* (4), 3411−3419.
(31) García-Santamaría, F.; Brovelli, S.; Viswanatha, R.; Hollingsworth, J. A.; Htoon, H.; Crooker, S. A.; Klimov, V. I. Breakdown of Volume Scaling in Auger Recombination in CdSe/CdS Heteronanocrystals: The Role of the Core−Shell Interface. *Nano Lett.* 2011, *11* (2), 687−693.
(32) Jain, A.; Voznyy, O.; Hoogland, S.; Korkusinski, M.; Hawrylak, P.; Sargent, E. H. Atomistic Design of CdSe/CdS Core−Shell Quantum Dots with Suppressed Auger Recombination. *Nano Lett.* 2016, *16* (10), 6491−6496.
(33) Hou, X.; Li, Y.; Qin, H.; Peng, X. Effects of Interface-Potential Smoothness and Wavefunction Delocalization on Auger Recombination in Colloidal CdSe-Based Core/Shell Quantum Dots. *J. Chem. Phys.* 2019, *151* (23), 234703.
(34) Oron, D.; Kazes, M.; Banin, U. Multiexcitons in Type-II Colloidal Semiconductor Quantum Dots. *Phys. Rev. B* 2007, *75* (3), 035330.
(35) Hou, X.; Qin, H.; Peng, X. Enhancing Dielectric Screening for Auger Suppression in CdSe/CdS Quantum Dots by Epitaxial Growth of ZnS Shell. *Nano Lett.* 2021, *21* (9), 3871−3878.
(36) Hou, X.; Kang, J.; Qin, H.; Chen, X.; Ma, J.; Zhou, J.; Chen, L.; Wang, L.; Wang, L.-W.; Peng, X. Engineering Auger Recombination in Colloidal Quantum Dots via Dielectric Screening. *Nat. Commun.* 2019, *10* (1), 1750.
(37) Zhao, T.; Beckwith, J. S.; Amin, M. J.; Palmai, M.; Snee, P. T.; Tien, M.; Yang, H. Leveraging Lifetime Information to Perform RealTime 3D Single-Particle Tracking in Noisy Environments. *J. Chem. Phys.* 2021, *155*, 164201.
(38) Zhong, X.; Feng, Y.; Knoll, W.; Han, M. Alloyed $Zn_xCd_{1-x}S$ Nanocrystals with Highly Narrow Luminescence Spectral Width. *J. Am. Chem. Soc.* 2003, *125* (44), 13559−13563.
(39) BenDaniel, D. J.; Duke, C. B. Space-Charge Effects on Electron Tunneling. *Phys. Rev.* 1966, *152* (2), 683−692.
(40) Otsu, N. A Threshold Selection Method from Gray-Level Histograms. *IEEE Trans. Syst. Man Cybern.* 1979, *9* (1), 62−66.
(41) Kay, S. M.*Fundamentals of Statistical Signal Processing, Vol. II: Detection Theory*; Prentice Hall: Upper Saddle River, NJ, 1998.
(42) Li, H.; Yang, H. Statistical Learning of Discrete States in Time Series. *J. Phys. Chem. B* 2019, *123* (3), 689−701.
(43) Watkins, L. P.; Yang, H. Detection of Intensity Change Points in Time-Resolved Single-Molecule Measurements. *J. Phys. Chem. B* 2005, *109* (1

https://doi.org/10.1021/acs.nanolett.2c03563
Nano Lett. 2022, 22, 9470−9476